Interactions between a fluctuating polymer barrier and transport factors together with enzyme action are sufficient for selective and rapid transport through the nuclear pore complex

Sunghan Ro, Ajay Gopinathan, and Yong Woon Kim

Phys. Rev. E **98**, 012403 — Published 5 July 2018

DOI: 10.1103/PhysRevE.98.012403

Interactions between a fluctuating polymer barrier and transport factors together with enzyme action are sufficient for selective and rapid transport through the nuclear pore complex

Sunghan Ro,[1,2] Ajay Gopinathan,[3] and Yong Woon Kim[1,2,*]

[1] *Department of Physics, Korea Advanced Institute of Science and Technology, Deajeon 34141, Korea*
[2] *Graduate School of Nanoscience and Technology, Korea Advanced Institute of Science and Technology, Deajeon 34141, Korea*
[3] *Department of Physics, University of California at Merced, California 95343, USA*

The nuclear pore complex, the only pathway for transport between the nucleus and cytoplasm, functions as a highly selective gate that blocks non-specific macromolecules while allowing the rapid transport of tagged (transport factor (TF)-bound) cargo up to an order of magnitude larger. The mechanism of this gate's operation is not yet fully understood and progress has been primarily hindered by the inherent complexity and multi-scale nature of the problem. One needs to consider the hundreds of disordered proteins (FG nups) lining the pore, as well as their overall architecture and dynamics at the microsecond scale, while also accounting for transport at the millisecond scale across the entire pore. Here we formulate an approach that addresses transport properties over a large range of length and time scales. We do this by incorporating microscopic biophysical details, such as charge and specific TF-FG nup interactions to compute the free energy landscape encountered by the cargo. We connect this to macroscopic transport by treating cargo translocation as a stochastic barrier crossing process and computing the current and the translocation time. We then identify distinct transport regimes (fast permeable, slow permeable, and impermeable) determined by the cargo size, TF affinity for FG nups and the activity of the enzymes that cleave TFs from cargo. Our results, therefore provide an integrated picture of transport through the NPC, while highlighting how FG nup interactions with TFs and enzyme activity cooperate to produce selectivity and efficiency.

I. INTRODUCTION

Nuclear pore complexes (NPCs) regulate material transport and genetic information flow across nuclear envelopes in eukaryotic cells [1, 2]. The NPC is a large macromolecular complex with more than thirty different protein types forming a structural ring that sits in the nuclear envelope surrounding a central pore. The central aqueous conduit of the pore is filled with hundreds of disordered nucleoporin proteins of more than a dozen different types, having phenylalanine-glycine motifs (FG nups) [3, 4], which form a highly selective barrier. Whereas small molecules traverse NPCs freely, large cargos selectively pass through NPCs only when they are bound to transport factors (TFs).

For decades, extensive experimental [5–20] and theoretical efforts [21–32] have been made to understand how NPCs display size selectivity while still allowing for the rapid transport of large TF-bound cargo. While it is clear that FG nups play a key role, no consensus has been reached on the underlying mechanism by which they contribute to selective gating.

The controversy in proposed mechanisms and the gap in our understanding largely originate from the lack of direct visualization of the conformations of disordered FG nups inside the NPC. As a consequence, most of the prominent existing models have had to consider hypothetical conformations based on indirect and sometimes contradictory experimental observations [9–20].

Most theoretical and computational studies to date, therefore, have focused on either (i) describing the kinetics of transport through simplified effective potentials [31] or highly simplified polymer models of the NPC [23, 29, 30] or (ii) addressing the polymer structure of the FG-nup barrier explicitly [24–27]. Studies that are in the former category do not take into account the role of biophysical details of sequence specific properties of the FG nups, such as hydrophobicity, electric charge and FG repeat distribution, while studies in the latter category lack quantitative predictions of experimentally measurable metrics that characterize the cargo transport. In order to gain a unified understanding, however, a theoretical model should ideally have the following features; (i) it should incorporate the salient biophysical features of FG-nup sequences. (ii) It should be able to predict experimentally verifiable conformations of the FG-nup assembly. (iii) Given these conformations, it should be able to quantitatively predict transport properties as functions of physical parameters of the system, such as cargo size, TF affinity for FG domains, and RanGTP concentration and kinetics. To date, however, there are no models that incorporate all these features, hence a full understanding of the physical mechanism behind selective gating is still missing.

In this work, we take the first steps towards constructing a statistical physics model of cargo transport through NPC where biophysical details of FG-nup sequence are incorporated at the residue level. Considering cargo transport as a stochastic process of crossing the free en-

* To whom correspondence should be addressed (e-mail: y.w.kim@kaist.ac.kr).

ergy barrier due to an assembly of fluctuating polymers allows us to address macroscopic transport through the pore in a quantitative fashion as a function of system parameters. In particular, we discover that highly selective, yet rapid transport, which has been a longstanding puzzle of NPC transport requires cooperativity between TF and RanGTP. To highlight the essential physics of the gating mechanism, we consider a minimal system with only one single type of FG-nup. This minimalist approach is inspired by the fact that size-selective transport has been observed in artificial nanopores with a single species of FG nup [33, 34] and furthermore, over half the FG-nup mass can be deleted *in vivo* with no loss of essential gating function [35]. We also indicate how our approach can be extended to consider the full complexity of the NPC, given the computational resources.

Adopting a polymer physics approach, we first describe the FG-nups as flexible polymers with interacting monomers on a coarse-grained level, while still taking into account the sequence-specific properties at the residue level, such as the hydrophobicity, electric charge, and FG repeat distribution. Using Monte Carlo simulations, we find that the FG nups undergo a conformational transition between open and closed states of the NPC as a function of the FG-FG interactions. Remarkably, at the transition point, the conformations are highly fluctuating, which is consistent with recent high-speed atomic force microscopy observations of the spatiotemporal behavior of FG-nup conformations inside the NPC [36]. We then examine the transport of cargo molecules through the NPC in the fluctuation-dominated regime, and quantify the transport properties in terms of the current and translocation time, which can also be measured in experiments. To do this, we compute, using the Jarzynski equality, the characteristic free energy barrier due to the FG-nups encountered by a cargo. Treating the transport as a stochastic barrier crossing problem [37, 38], we determine the values of the cargo size and TF-FG interaction strength for efficient cargo transport and show that a size exclusion limit naturally arises and that higher TF affinity can increase the size limit of allowed cargo. We also point out the role of RanGTP, which unbinds TF from a cargo inside the nucleus. Although TFs enhance the currents of cargo molecules, we show that without RanGTP, the cargo transport can be very slow. Upon addition of RanGTPs, translocation can speed up, indicating that efficient cargo transport through the NPC is a result of an orchestrated action of TF and RanGTP.

II. METHODS

As natively-unfolded flexible linear chains with weakly-interacting multiple sites, FG nups are modeled as freely-jointed chains of N connected spherical monomers of diameter a each. The hydrophobicity and electric charge of the amino acids in the FG nups are taken into account via hydrophobic, electrostatic, and steric interactions among the monomers. As a compromise between biophysical details and computational costs, we introduce a coarse-grained mesoscopic model in which six consecutive amino acids constitute a single monomer. A monomer is categorized as hydrophobic, hydrophilic or neutral, following the Honeycutt-Thirumalai model [39, 40], and the electric charge of a monomer is given by the sum of the charges of the six amino acids. Details of this procedure and the interaction potentials between monomers are given in Appendix A and B. For various FG nups, this mesoscopic model yields radii of gyration, R_g, which are comparable with values measured in experiments (see Appendix B). As a representative FG nup, we choose Nsp1, the most abundant yeast nucleoporin. These FG nups (Nsp1) are grafted with 8-fold symmetry inside an NPC, which is regarded as a cylindrical pore of radius R_{pore}. Here, R_{pore} is set to be $25a$, leading to $R/R_g(\mathrm{Nsp1m}) = 3.55$, which is comparable to experimental values (see Appendix B). Using the Metropolis algorithm, we perform Monte Carlo simulations in which the equilibrium configurations of the FG nups are efficiently sampled via various moves, such as monomer rotation, pivot, crank, and pivot cluster (see Appendix A.4 for details). To evaluate the free energy barrier for translocation, we employ the Jarzynski equality [41–43], which allows us to quantitatively calculate the free energy difference using non-equilibrium work measurements in simulations. We model the translocation dynamics of cargo by a pair of coupled Fokker-Planck equations describing probability densities of bare cargo and TF-cargo complexes. The current and translocation time of the cargos are then calculated by numerically solving these equations [44].

III. RESULTS

A. Conformational transitions and fluctuations

We first look at the conformations of FG nups in the absence of a cargo-TF complex, as shown in Fig. 1a. The conformations are very sensitive to the strength of hydrophobic interaction between monomers, ε. Hereafter, all energies and lengths are expressed in units of the thermal energy at room temperature k_BT and of the monomer diameter a, respectively. For weak hydrophobic interaction ($\varepsilon = 1.0$), the chains mostly populate the inner rim of the NPC, have low inter-chain connectivity, and form isolated brush-like configurations. On the other hand, at high interaction strength ($\varepsilon = 2.4$), the strong cohesion between the hydrophobic monomers causes the chains to aggregate and form a central plug. For an intermediate value, $\varepsilon = 1.7$, the inter-chain aggregation is enhanced compared to the case of $\varepsilon = 1.0$, and yet the central region is less crowded than the case of $\varepsilon = 2.4$.

In order to quantify the configuration of the FG nups,

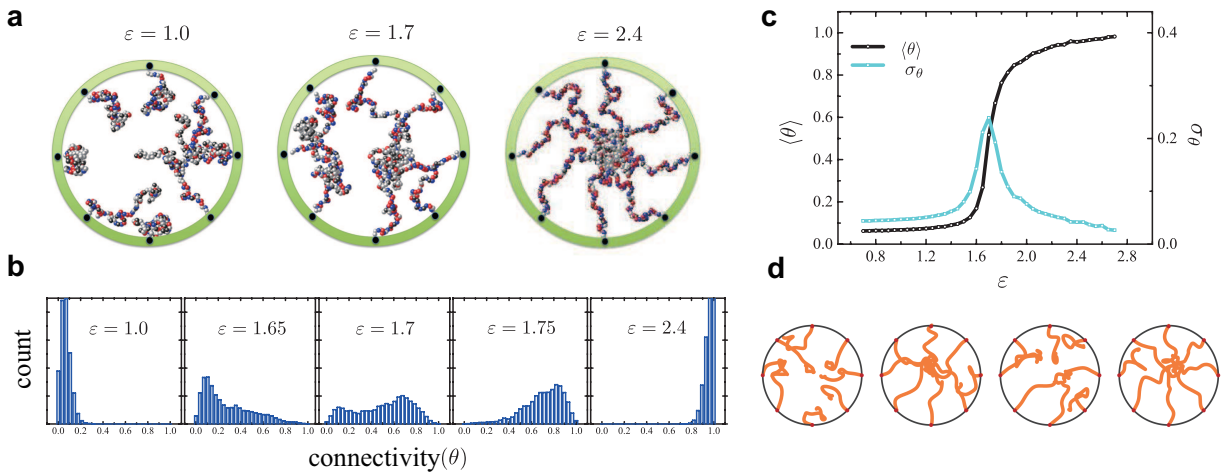

FIG. 1. (a) Snapshots (top view) of FG nups from simulations for various hydrophobic interaction strengths ε. Different colors indicate physical properties of monomers; hydrophobic (dark gray), negatively charged (blue), positively charged (red), and electrically neutral (light gray). For weak interactions ($\varepsilon = 1.0$), FG nups are isolated resulting in an open NPC. For increasing interaction strengths, FG nups are partially entangled ($\varepsilon = 1.7$), or form a central plug ($\varepsilon = 2.4$). (b) Occurrence counts of the FG nup configurations having connectivity θ, defined in Eq. (2), showing how the typical configurations change from the open state to the closed state as ε increases. For intermediate ε ($\varepsilon = 1.7$), the connectivity of FG nups has a bimodal distribution. (c) The average connectivity $\langle\theta\rangle$ and its fluctuation $\sqrt{\langle\theta^2\rangle - \langle\theta\rangle^2}$ vs. ε. Near $\varepsilon = 1.7$, $\langle\theta\rangle$ rapidly changes, signaling a conformational transition that is accompanied by pronounced fluctuations. (d) Configurations of FG nup at $\varepsilon = 1.7$, represented by thick orange lines, closely resemble the conformational fluctuations observed in recent experiments [36].

we introduce a connectivity matrix,

$$C_{\alpha\beta} \equiv \begin{cases} 1 & \text{if } d_{\alpha\beta} \le r^*, \\ 0 & \text{otherwise,} \end{cases} \tag{1}$$

where α, β are chain indices; we assign $C_{\alpha\beta} = 1$ if the smallest separation between monomers in chain-α and those in chain-β, denoted by $d_{\alpha\beta}$, is less than $r^* = 2.5a$. Using the connectivity matrix, we define the connectivity of the whole system as an order parameter:

$$\theta \equiv \frac{2}{N_c(N_c-1)} \sum_{\alpha=1}^{N_c} \sum_{\beta=1}^{\alpha-1} C_{\alpha\beta} \tag{2}$$

which becomes zero if all chains are isolated; this value is unity when all chains are interconnected with each other. Here, the number of chains in the system is $N_c = 8$.

Figure 1b presents the probability distribution of the connectivity θ. For small $\varepsilon = 1.0$, the probability is sharply peaked near $\theta = 0$, clearly indicating that the majority of the chains has very low connectivity. For an enhanced strength, $\varepsilon = 1.65$, the peak becomes lowered, and the probability leaks into the large θ region. At $\varepsilon = 1.7$, the probability distribution is bimodal, suggesting that the chain conformations fluctuate significantly between connected and disconnected states. With further increase of ε, a peak is developed near $\theta = 1$ and finally becomes very sharp at $\varepsilon = 2.4$, which is in accordance with the chain configurations displayed in Fig. 1a.

In Fig. 1c, we display the average connectivity $\langle\theta\rangle$ and the standard deviation $\sigma_\theta = \sqrt{\langle\theta^2\rangle - \langle\theta\rangle^2}$ as a function of the hydrophobic interaction strength ε. For $\varepsilon < 1.6$, the average connectivity remains small (sparsely connected; open phase). As ε increases, the connectivity becomes larger, and for $\varepsilon \ge 2.0$, the connectivity converges to 1 (fully connected; closed phase). The rapid rise of the order parameter, $\langle\theta\rangle$, at $\varepsilon = 1.7$; signals a sharp conformational transition of the FG nups.

The transition found here [Fig. 1c] is also accompanied by pronounced conformational fluctuations (see σ_θ, which has a sharp maximum at the transition point). At $\varepsilon = 1.7$, therefore, the isolated brush-like conformations and transient entanglements coexist. The snapshots of the configurations at that point (Fig. 1d) closely resemble those observed in the experiment by Sakiyama *et al.* (Compare with Fig. 2a of Ref. [36]). Motivated by this experimental observation, in the remainder of this work, we will assume a hydrophobic interaction strength of $\varepsilon = 1.7$, for which the fluctuations are the most pronounced. We next compute explicitly, the free energy barrier due to the fluctuating FG nup assembly, and show how selective transport arises in our model NPC.

B. Free energy barriers of translocation modulated by TF-FG nup interactions

In order to model the transport process, we first quantitatively estimate the free energy barrier that a cargo molecule experiences when passing through our model NPC [Fig. 2a]. In obtaining such free energies, a scheme based on the Jarzynski equality [41] is useful, as was

successfully demonstrated in many biomolecular systems such as the folding-unfolding of RNA molecules [45, 46]. Here, we use the Jarzynski equality to calculate the free energy barrier as a function of the translocation coordinate, z (position of cargo). Consider a process in which a cargo located at a position z_0 moves to another position $z > z_0$. During the process, finite work, w, should be expended due to the interaction between FG nups and the cargo, which depends on the cargo position. The Jarzynski equality states that the exponential average of the work determines the difference in the free energies at z_0 and at the final position z:

$$e^{-\beta \Delta F} = \langle e^{-\beta w} \rangle_w, \tag{3}$$

where $\Delta F = F(z) - F(z_0)$, and $\langle \cdots \rangle_w$ represents the average with respect to the probability of w. Here $F(z)$ is the free energy of the system when the cargo is located at z. The above relation (3) can be used to evaluate the free energy profile as a function of the cargo position (see Appendix C for details). We choose a reference value of z_0 far enough away from the pore center so that the free energy approaches the bulk value, to which FG nups do not contribute.

When the cargo, taken to be a spherical particle of radius R, does not contain a nuclear localization signal, it does not bind to TF and is therefore regarded as an inert particle interacting with FG nups only sterically due to its finite volume. On the other hand, if the cargo binds to TF, it forms a cargo-TF complex, also referred to here as an interacting cargo. The presence of bound TF is modeled as $N_b = 12$ binding sites arranged in a stripe pattern on the cargo (see Supplementary Information). The binding sites interact specifically with FG repeats along the nups, the strength of which can be parameterized by ε_{TF}. As most TFs are strongly negatively charged in physiological conditions [47], the binding sites are also assumed to carry the electric charge $q = -5e$ per site, giving total charges of TF of $Q = -60e$. As a result, the cargo-TF complex interacts with FG nups not only through steric repulsion but also through electrostatic and hydrophobic interactions (for details, see Supplementary Information).

Figures 2b-c present the free energy barrier for cargo translocation, obtained after performing a number of repeated measurements of work and then taking the average of the exponentiated work values according to the Jarzynski equality, (3), (details in Appendix C). As an inert cargo without TF passes through an NPC, due to the entropic repulsion with the FG nups, a free energy barrier develops symmetrically around the anchoring position of the FG nups, $z = 0$. The entropic penalty and the resulting free energy barrier are higher for a larger cargo, as shown in Fig. 2b. For a cargo-TF complex, on the other hand, the attractive electrostatic and hydrophobic interactions with the FG nups lower the free energy barrier compared to that for an inert molecule. Figure 2c illustrates the free energy landscape for various ε_{TF}. It is interesting to notice that the wells in the free energy,

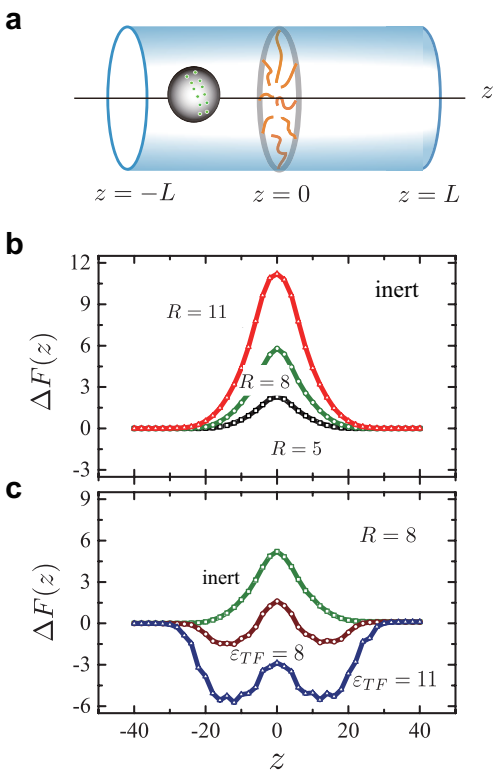

FIG. 2. (a) Schematic of a spherical cargo translocating through a model NPC with FG nups anchored at $z = 0$. (b) Free energy difference, $\Delta F(z) = F(z) - F(z_0)$, as a function of the cargo position z, for inert cargo ($\varepsilon_{TF} = 0$) of radius ($R = 5, 8, 11$). Here, $z_0 = -40$. A free energy barrier is developed around the anchoring position of the FG nups due to steric interactions between the cargo and the FG nups. Consequently, the barrier is higher for a larger cargo. (c) Free energy profiles of interacting cargo of radius $R = 8$ with different ε_{TF}. For the interacting cargo, not only is the barrier at $z = 0$ lowered, but also wells (the regions of $\Delta F < 0$) are created.

the regions having $\Delta F < 0$, develop for elevated ε_{TF}, which leads to a trapped state of the cargo-TF complex inside an NPC. Their role in the transport process will be discussed in the next section. The total binding energy between a TF and the FG nups, measured from simulations as shown in Fig. 2c, is about $10 \sim 20 k_B T$, which appears to be compatible with the range of experimentally measured binding affinity of nM $\sim$ μM [48–51]. We also note that translocation potentials having both barriers and wells were reported through mean-field calculations of the potential of mean force [24, 25]. While a single layer of FG nups is considered in our work, the asymmetric distribution of the FG nups consisting of several layers of different types were incorporated in these previous studies [24, 25], leading to asymmetric free energy barriers of translocation. Such comprehensive treatments of the potentials of mean force can easily be incorporated into our approach by using these as the starting point for the free energy landscape in what follows. What is being

pursued in this study is a systematic analysis of the effects of ε_{TF} and R on the translocation free energy *due to a highly fluctuating polymer barrier* and the resulting translocation dynamics which in turn depends also on the RanGTP concentration and kinetics.

C. Dynamics of crossing the free energy barrier

In most experiments, transport across the NPC is studied by measuring the flux or translocation time of the cargo molecules. Here we calculate these transport quantities based on a stochastic description of cargo translocation. In doing so, two crucial factors are considered. First, because translocation time scales are much longer than the relaxation times of polymers (on the order of μsec) [52], the cargo position, z, is a slow stochastic variable. We can then consider the translocation of cargo as a one-dimensional diffusive random process across the free energy barrier arising from interactions with FG nups [10, 31]. Second, we note that the directionality of cargo transport through NPC is maintained *in vivo* by the hydrolysis of GTP by GTPase Ran [53]. When binding to the cargo-TF complex, RanGTP, which is mainly present inside the nucleus, dissociates TF from a cargo and releases the cargo into the nucleoplasm [10]. We account for the action of RanGTP by a second-order chemical reaction in which RanGTP binds to the cargo-TF complex.

We can then write the Fokker-Planck equations describing the translocation dynamics:

$$\begin{aligned}\frac{\partial}{\partial t}p(z,t) &= \mathcal{L}_{\rm FP}(z)p(z,t) - k_{on}c(z)p(z,t) \\ \frac{\partial}{\partial t}q(z,t) &= \mathcal{L}^0_{\rm FP}(z)q(z,t) + k_{on}c(z)p(z,t)\ ,\end{aligned} \tag{4}$$

where the Fokker-Planck operators are given, respectively, as $\mathcal{L}_{\rm FP} = D(\partial/\partial z)\exp\left[-F(z)\right](\partial/\partial z)\exp\left[F(z)\right]$ and $\mathcal{L}^0_{\rm FP} = D(\partial/\partial z)\exp\left[-F_0(z)\right](\partial/\partial z)\exp\left[F_0(z)\right]$ with a diffusion constant D. Here, $p(z,t)$ is the one-dimensional density of the cargo-TF complex, while $q(z,t)$ is one-dimensional density of the cargo in the TF-free state, i.e., dissociated from TF by RanGTP. The concentration of RanGTP is denoted by $c(z)$; the localization of RanGTP in a nucleus can be approximately described by a Heaviside step function, $c(z) = c_0\Theta(z)$. Here, k_{on} is the probability that a cargo-TF complex will converted by RanGTP into a TF-free state per unit time, from which we obtain a normalized rate constant, $k = k_{on}c_0$. The terms coupled to $c(z)$ are introduced to incorporate the annihilation of a cargo-TF complex (or equivalently the production of a TF-free cargo). Note that the free energy profile $F(z)$ enters Eq. (4), and $F_0(z)$ is the free energy experienced by a TF-free cargo, which is treated as an inert particle: $F_0(z) = F(z;\varepsilon_{TF} = 0)$.

The advantage of our approach is that transport quantities such as flux and translocation time can be directly evaluated from the Fokker-Planck equation when appropriate boundary conditions are imposed. To evaluate the current and the translocation time, we consider a cargo molecule translocating from the *cis* side to the *trans* side, i.e., from the cytoplasm to the nucleoplasm, in the interval $[-L, L]$. In solving (4), we impose four boundary conditions:

$$\begin{aligned}p(z=-L,t) = p_0,\ p(z=L,t) = 0, \\ q(z=-L,t) = 0,\quad q(z=L,t) = 0,\end{aligned} \tag{5}$$

where $L = 40$, far distant from the pore center. For a cargo-TF complex, we assume a constant concentration at $z = -L$ (corresponding to the cargo-TF concentration in the cytoplasm) and an absorbing boundary at $z = L$, which assumes that, due to the high binding affinity of RanGTP for TF, TF is almost perfectly dissociated from cargo by RanGTP by the time the cargo reaches the nucleoplasmic face of the NPC. For an unloaded cargo, absorbing boundaries are assigned at both ends. It is to be noted that an arbitrary boundary value can be used for q, without changing currents, but only if the same value is used on both sides. TF-free cargos result only from dissociations of cargo-TF complexes so, initially, $q(z,0) = 0$.

At steady state, the current is given by

$$J = -D\left(\nabla p_s(z)|_{z=L} + \nabla q_s(z)|_{z=L}\right),$$

and the translocation time can be estimated as the total number of cargos divided by the current:

$$\tau = \frac{1}{J}\int_{-L}^{L} dz\left[p_s(z) + q_s(z)\right], \tag{6}$$

where $p_s(z)$ and $q_s(z)$ are the steady state solutions of (4) with $\partial p(z,t)/\partial t = 0$ and $\partial q(z,t)/\partial t = 0$. Thus, by numerically solving (4) with the appropriate boundary conditions (5) [44], we can obtain the currents and translocation time for a wide range of parameters. It should be noted that there exists a similar mechanism, involving a different set of TFs and enzymes, for export to the cytoplasm, so that nuclear export can be described by our formalism as well by simply considering the *cis* (*trans*) side as the nucleoplasm (cytoplasm).

D. Flux and transit time explain size-selective permeability: transport in the absence of RanGTP

Let us first examine the translocation behaviors in the absence of RanGTP. In this case, we set $k = 0$ or, equivalently, $c(z) = 0$, in (4) and solve the equation with the free energy $F(z)$ evaluated as explained in Sec. III. For numerical calculations, the diffusion constant is taken as $D = k_BT/6\pi\eta R$ with the viscosity of cytoplasm η; the monomer diameter is $a = 1$nm. Since the current is linearly proportional to p_0, the concentration gradient between the *cis* and *trans* sides, we consider, in the following, a normalized current JA/p_0 with a pore area A. In

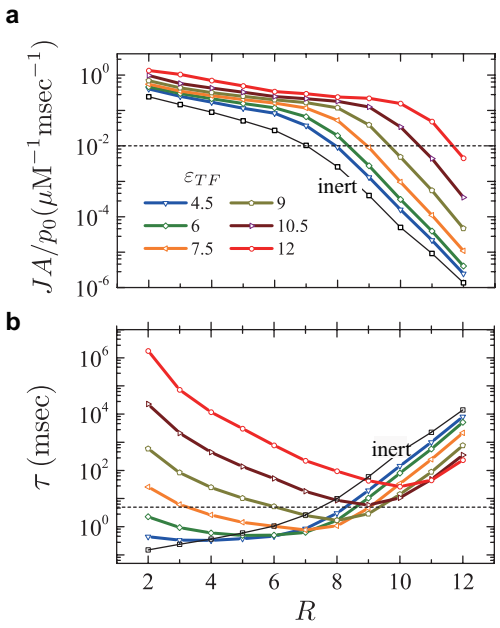

FIG. 3. Current and translocation time of cargo through our model NPC (obtained numerically as described in Sec. III.C). We set $k = 0$ and $p_0/\pi R_{pore}^2 = 1\mu$M. (a) Current J as a function of the cargo radius R. At a given ε_{TF}, the currents are reduced as R increases. At a given radius, cargos more strongly interacting with FG nups yield larger currents. In the R-dependence of J, there exists a crossover from slow to fast decay that represents the size-selective permeability. The dashed line corresponds to the current amplitude at the crossover for an inert cargo. (b) Translocation time τ as a function of R. For an inert cargo, τ monotonically increases with R; its dependence on R also displays crossover behavior (the dashed line is the translocation time at the crossover). In contrast to the inert cargos, the translocation times of interacting cargos have minima. The descending behavior of τ for small R is a consequence of the well formation shown in Fig. 2(c).

Fig. 3, we present the currents JA/p_0 for $p_0/A = 1\mu$M and the translocation times τ as functions of R for various values of ε_{TF}.

One immediately finds that the currents diminish with increasing cargo radius (Fig. 3a); moreover, there exists a crossover in the R-dependence, from a weak $1/R$-dependence to a rapid exponential decay ($\ln J \sim -R$). The crossover enables sharp changes in permeability depending on the cargo radius and forms the basis of size-selective permeability in the NPC. The dependence of the currents on ε_{TF} is also noteworthy here. As $\varepsilon_{\mathrm{TF}}$ is enhanced, overall, the amplitude of the current and the threshold radius increase. This behavior can be understood by looking at the free energy barrier in Fig. 2c; its height at $z = 0$ is lowered for an interacting cargo, compared with that for an inert cargo ($\varepsilon_{TF} = 0$); this value becomes even lower at higher ε_{TF}.

Another relevant quantity is the translocation time for a single cargo, τ, presented in Fig. 3b. For an inert cargo, τ monotonically increases as R becomes larger; this is obviously due to the steric repulsion yielding a higher barrier for a larger cargo (see Fig. 2b). In contrast, the translocation time for interacting cargo displays a non-monotonic behavior with increasing cargo radius, having a minimum value at an optimal cargo size. The counter-intuitive behavior of τ before the minimum point where translocation time decreases with size is a consequence of well formation in the free energy landscape for interacting cargos (Fig. 2c). The overall translocation dynamics is governed not only by the barrier height at the center but also by the well depth at the nuclear side exit. Thus, in the case of a strongly-trapped cargo, the rate-limiting step in translocation is the escape from the well, not the barrier crossing. Up to the minimum point, as R increases, the well depth becomes smaller; as a result, τ decreases. For further increases in R, the central barrier crossing becomes the rate-limiting step, and τ increases. The upturn in τ also coincides with the crossover in permeability indicated by the marked reduction of the currents displayed in Fig. 3a.

In Fig. 4a, we summarize the translocation behavior as a function of TF affinity, ε_{TF}, and cargo size, R. Here, we choose the reference current, $J^* = 0.01/\mathrm{msec} \cdot \mu\mathrm{M}$, for the value separating impermeable ($J < J^*$) and permeable ($J > J^*$) regions. Comparing the translocation time with a reference time $\tau^* = 5$msec, the permeable region is further divided into two; slow ($\tau > \tau^*$) and fast ($\tau < \tau^*$). Based on the current and translocation time behaviors of inert cargo, these criteria (dashed lines Fig. 3) are chosen as values around the crossover, and are found to be close to the values that were experimentally measured [54, 55] (e.g., J^* corresponds to the current at which ten molecules pass through a pore per sec when the cargo concentration on the *cis* side is given as 1μM). For example, as shown in Fig. 3, inert cargos with $J > J^*$ and $\tau < \tau^*$ have flux and translocation time that depend weakly on their radii, and we classify the transport to be permeable and fast. To some extent, the determination of reference values can be arbitrary; if we consider the cutoff current to be ten times larger (corresponding to passage of hundred molecules per sec), the impermeable region expands and the boundary is thus shifted as shown Fig. 3a. We note, however, that the behaviors of boundaries are qualitatively the same.

The diagram clearly shows that with increasing ε_{TF}, the size cutoff in permeability shifts to a larger value. This indicates that the transport of large cargos, which would be blocked without TF, is allowed by binding TFs. However, even if permeable, the transport can be slow for small cargos with large ε_{TF} (Slow Permeable region), because the cargo tends to be strongly trapped by strong interactions of the TFs with FG nups. We will now show that the presence of RanGTP, which was neglected in Fig. 4a, has a nontrivial effect on reducing the translocation time.

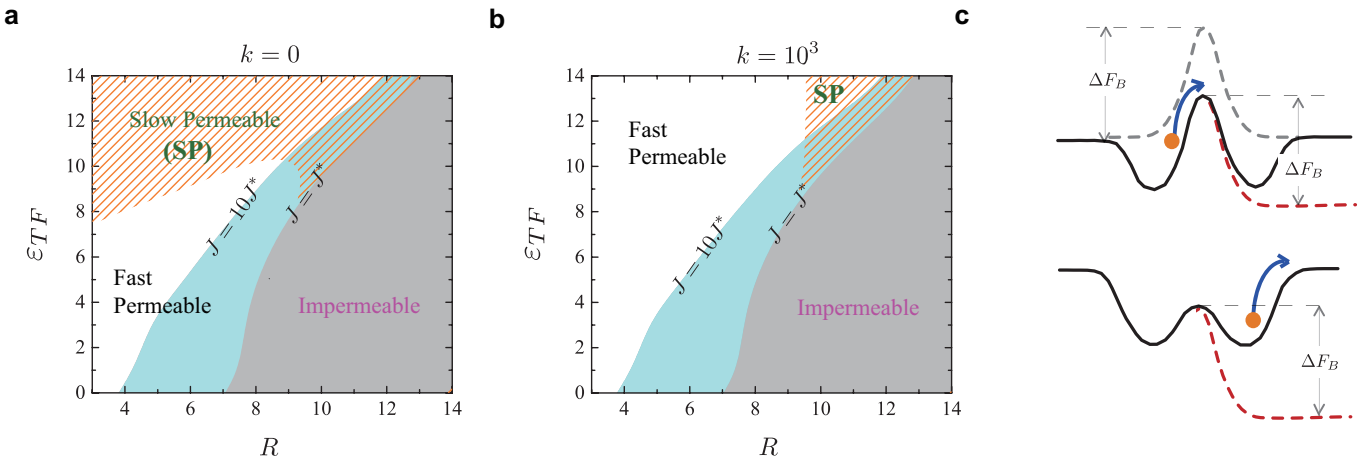

FIG. 4. Diagrams to characterize the cargo transport through NPC (a) in the absence of RanGTP ($k = 0$) and (b) in the presence of RanGTP ($k = 10^3$) based on current and translocation time obtained numerically as described in Sec. III.C). Cargos with R and ε_{TF} in the fast permeable region are efficiently transported through NPC, yielding high currents and short translocation time $\tau < \tau^*$. Boundaries between permeable and impermeable regions are indicated by setting $J = J^*$ or $J = 10J^*$, respectively. Here the criteria J^* and τ^* are marked in Fig. 3. (c) Schematic pictures of free energy profiles of translocation for inert cargo (gray dashed), and interacting cargo without RanGTP (black solid) and with RanGTP (red dashed). Here ΔF_B is the central barrier height for an inert cargo. On the *trans* side, RanGTP dissociates a cargo from TF and replaces the free energy profile with that for an inert cargo. (Upper panel) The rate-limiting process is the crossing of the central barrier; therefore, the presence of RanGTP hardly affects the translocation time. (Lower panel) For a strongly-trapped cargo inside the well, the rate-limiting process is the escape from the well. In this case, the presence of RanGTP accelerates the translocation.

E. RanGTP speeds up translocations: cooperativity of RanGTP and TF

The effects of RanGTP can be examined by using finite values of k in (4). The RanGTP concentration in the nucleus is taken as $c_0 = 10\mu$M [56]. Numerically solving (4) with BCs (5) [44], we obtain the currents and translocation time for a wide range of k. We find that the permeability boundaries determined by J remain almost unchanged with increasing k, though the relative contributions of cargo-TF complex and dissociated cargo to the current change drastically as k varies. On the other hand, the translocation time τ for small cargo continuously decreases upon addition of RanGTP (or with increasing k), but remains higher than τ^* till k reaches a certain threshold value. Up to this point, therefore, the boundaries, (set by τ^*) separating the slow and the fast regions, stay close to those for the case of $k = 0$ (no RanGTP). As k increases above the threshold value, $\sim k = 10^3$, the fast region suddenly expands and takes over most of the permeable domain (Fig. 4b). We also find that even if k increases further, there is no qualitative change in the boundary of τ (see Appendix D, Fig. 9).

This sensitive dependence of the phase boundary of τ on k is a consequence of how RanGTP affects the free energy of translocation. RanGTP unbinds TF from a cargo-TF complex and as a result, the free energy landscape of a dissociated cargo on the *trans* side becomes equivalent to the free energy of an inert cargo [Fig. 4c]. For large cargos with considerable barriers at the center, as well as negative wells on both sides [upper panel of Fig. 4c], RanGTP plays the role of removing the activation barrier at the nucleoplasm exit. However, in this case, surmounting the central barrier from the *cis* side is the rate-limiting step, which is unaffected by addition of RanGTP. Consequently, both J and τ hardly change. On the other hand, for small cargos with large ε_{TF}, which have deep wells in the free energy landscape [lower panel of Fig. 4c], traversing the activation barrier at the nucleoplasm exit forms the rate-limiting step. RanGPT removes this activation barrier and the translocation, therefore, speeds up significantly. In contrast, RanGTP has only a negligible effect on the currents. Note that as the potential well disappears on the *trans* side, cargo density becomes reduced. Because the current is the cargo density multiplied by the translocation speed, the speed-up effect and the density reduction caused by RanGTP cancel each other out, yielding almost the same currents as those in the absence of RanGTP. It appears that RanGTP lowers the free energy of the product state without modulating the central barrier; RanGTP is distinct in that sense from a classical Michaelis-Menten enzyme that simply reduces the activation energy barrier.

Thus, there are two key findings in our results about the role of RanGTP. First, RanGTP makes the cargo translocation fast and complements the role of TF, which enhances the cargo permeability. Second, in order for the speed-up effect of RanGTP to manifest itself, i.e., to reduce τ below τ^*, RanGTP should be sufficiently abun-

dant to realize a value of k beyond a certain threshold value. However, because this effect is saturated for values of k larger than the threshold value, any RanGTP, which exists in quantities more than necessary, becomes a surplus agent. Given $c_0 = 10\mu$M [56], $k = 10^3$ corresponds to an on-rate of $k_{on} = 10^8/\text{M}\cdot\text{sec}$ [57], which is much higher than the on-rate value measured *in vitro* of $\sim 10^5/\text{M}\cdot\text{sec}$. It was found, however, that this on-rate of $\sim 10^5/\text{M}\cdot\text{sec}$ is too slow to explain the import kinetics, and that RanGTP binding to Impβ should occur at least one to two orders of magnitude faster [58], which will make the on-rate much closer to the threshold value used in this work. Other NPC-associated components have indeed been shown to increase this on-rate significantly [59].

IV. DISCUSSION

Employing a statistical physics approach combined with polymer physics, we have investigated the physical mechanism of selective material transport through NPCs. Incorporating the biophysical details of FG nup sequence, we have determined the equilibrium conformations of FG nups as a function of the hydrophobic interaction strength, and have observed sharp conformational transitions, accompanied by pronounced fluctuations. Depending on the cargo size and the binding strength of TF with FG domains, the free energy landscape can be either a positive barrier, a trapping well, or a combination of both. As a result, different transport behaviors emerge; fast permeable, slow permeable or impermeable. Based on a reaction-diffusion equation, we have shown that the current exhibits a crossover behavior, changing from a slowly decaying to a rapidly decaying function of the cargo radius, which sets a natural size cutoff in permeability at the crossover radius. Having TFs bound to the cargo shifts the size cutoff to a larger value, allowing larger cargo to be translocated. In addition to maintaining the concentration gradient of molecules across the nuclear membrane, we found that RanGTP plays an important role in the translocation dynamics. Modulating the free energy landscape on the *trans* side, RanGTP can accelerate the translocation of a strongly-trapped particle that otherwise would stagnate inside an NPC. Size-selective and fast transport through the NPC is, therefore, achieved through cooperation between the TFs and RanGTPs.

It should be noted that, recently, there have been experiments which have focused on the additional biochemical activities of RanGTP in transport regulation, other than just the dissociation of TF from a cargo-TF complex. Lowe *et al.* proposed that RanGTP dissolves a highly cross-linked mesh formed by interactions of Impβ with nups at the nuclear face of the NPC [60]. According to their arguments, active transport should occur only when both TFs and RanGTPs are present, which is, however, incompatible with a previous report by Ma *et al.* where facilitated transport of large cargo was observed even in the absence of RanGTPs [7]. On the other hand, the Kap-centric control model in Ref. [61] suggested that RanGTP does not completely dissociate Kapβ1 from FG nups but instead switches Kapβ1 to a lower affinity state. In our analysis, we do not consider such molecular details of RanGTP-TF interactions and only assume the well-established fact that RanGTP unbinds cargo from TF to facilitate its release from FG-repeat regions. Our theoretical approach can easily be extended to include the detailed interactions between TF and RanGTP. While this will not change the main mechanism shown in our study, such an effort could be helpful to quantitatively test the various proposed models on the role of RanGTP.

We have shown here that the FG nup assembly in the NPC shows a conformational transition upon variation of the FG nup interaction energy, and proceeded to determine the transport properties of inert and TF-bound cargoes in pores using the FG nup interaction energy that accompanies the transition point. Whereas no simulations were performed to compare the transport properties of inert and TF-bound cargoes between pores employing different FG nup interaction energies, we note that the FG nups *in vivo* appear to be close to the transition point accompanied by the pronounced FG nup fluctuations [36]. The fluctuations could potentially play an important role by simultaneously providing a free energy barrier while allowing for only transient interactions with TFs, thus accelerating the dynamics and preventing trapping. The gating mechanism thus displays elements of various models proposed before including an entropic brush [11], a dynamic gel in the center [12, 21] and a copolymer gate that shows conformational transitions [20, 27, 30]. The predicted time-averaged polymer densities are also consistent with a high density center measured by both cryo-EM [62] and conventional AFM [63] while the fluctuating chain conformations are also consistent with the recent high-speed AFM measurements [36]. Interestingly, values for currents and transport times, on the order of $0.01/\text{msec}\cdot\mu$M and 5msec, that are consistent with direct measurements using cargo tracking with single molecule fluoresence techniques [54], appear to mark the boundaries between regimes where these quantities are weakly and strongly dependent on cargo size, indicating that the crossover may be exploited *in vivo*.

As final remarks, we address some aspects of the present work that can be improved in future studies. Here, we focused on translocation through a central conduit filled with flexible FG nups, not on the cytoplasmic or nucleoplasmic sides with cytosolic fibrils and the nuclear basket. The initial docking or interaction with the cytoplasmic filaments was regarded as a separate process and was excluded from this study. We also assumed that the free energy barrier of translocation through NPC results from the FG nups alone, in the absence of other factors. The contributions of other translocating molecules and cargo-cargo interactions were neglected, which would be valid at dilute concentrations. At high concentrations

of free Kaps for example, Kap-FG nup interactions have been shown to modulate the FG nup conformations [64–66] and this is something that could be included in extensions to this work. We also incorporated the effects of RanGTP by introducing the normalized rate constant k in the Fokker-Planck equations. It would be interesting to confirm the roles of RanGTP, associated with the changes of the free energy barrier as explained schematically in Fig. 4c, directly through the Monte Carlo simulations considering RanGTPs. In this study, a single ring of FG nups is considered, which enables us to span a wide range of the parameter values of R and ε_{TF} within reasonable computational time. The NPC however contains several such rings of different FG nup types and it is expected that the repulsive free energy barrier becomes higher and wider. As a result, the amplitudes of barrier height and well depth will change, but the overall shapes of the free energy landscape should remain roughly similar. Such free energy barriers for the NPC have indeed been calculated at different levels of approximation for the FG nup structure [24, 25] and it would be interesting to extend our transport calculations to free energy barriers calculated for the full pore. It has also been reported [67] that there could be co-operativity between different types of FG nups in regulating transport and this would be another aspect to include.

ACKNOWLEDGEMENTS

This research was supported by a National Research Foundation of Korea (NRF) grant funded by the Korean government (Grant No. NRF-2017R1A2B4007608). S. R. also acknowledges support from the NRF-2013-Global Ph.D. Fellowship Program (Grant No. NRF-2013H1A2A1033074). AG was partially supported by National Science Foundation NSF grant EF-1038697 and NSF grant DMS-1616926, a James S. McDonnell Foundation Award and in part by the NSF-CREST: Center for Cellular and Bio-molecular Machines at UC Merced (NSF-HRD-1547848).

Appendix A: System and simulation method

1. FG nups

Let us first introduce a model NPC system in the absence of cargos. Our minimal NPC is modeled as eight FG nups anchored, along the perimeter of a circle, inside a cylindrical pore of radius R_{pore}. The anchoring points of the FG nups are equally spaced to have eightfold rotational symmetry. Each FG nup is considered as a freely-jointed chain (FJC) of N spherical monomers of diameter a. The monomers occupy finite volume, carry charges, and have hydrophobicity, thus interacting with each other through steric, electrostatic and hydrophobic potentials.

The pairwise potential between the i-th and the j-th monomers is given as

$$U_{ij} = \phi^{st}(r_{ij}) + \phi_{ij}^{Coul}(r_{ij}) + \phi_{ij}^{hyd}(r_{ij}), \tag{A1}$$

where r_{ij} is the distance between the two monomers as $r_{ij} = |\mathbf{r}_i - \mathbf{r}_j|$ when the position vector of the i-th monomer is $\mathbf{r}_i$. The first term ϕ^{st} accounts for the steric repulsion of two monomers having finite radii and is given by

$$\phi^{st}(r) = \begin{cases} 4\varepsilon_{\rm LJ}\left[\left(\frac{r_0}{r}\right)^{12} - \left(\frac{r_0}{r}\right)^{6} + \frac{1}{4}\right] & \text{if } r \le r^* \\ 0 & \text{if } r > r^* \end{cases}, \tag{A2}$$

which is the truncated Lenard-Jones potential with $r^* = 2^{1/6} r_0$. Here, r_0 and $\varepsilon_{\rm LJ}$ are taken as a and $k_B T$, respectively. The second term in Eq. (A1) accounts for the electrostatic interaction between monomers, for which we introduce the screened Coulomb potential with the interaction range set by the Debye screening length λ_D:

$$\phi_{ij}^{Coul}(r) = \frac{q_i q_j}{4\pi\epsilon} \frac{e^{-r/\lambda_D}}{r} \tag{A3}$$

with ϵ being the dielectric constant of the ambient medium, where q_i, q_j are the electric charges of the monomers. At physiological salt concentrations, the Debye screening length is $\lambda_D = 1$nm. The last potential represents the effective hydrophobic/hydrophilic interaction, arising from the hydrophobicity of amino acid residues or monomers, which is modeled by an exponential function

$$\phi_{ij}^{hyd}(r) = \begin{cases} \sigma_{ij} e^{-(r-a)/\lambda_h} & \text{if } r > a \\ \sigma_{ij} & \text{if } r \le a \end{cases} \tag{A4}$$

with the decay length of the interaction of the size of monomer, $\lambda_h = a$ [68]. According to the Honeycutt-Thirumalai model [39, 40], the hydrophobicity of a monomer is assumed, for simplicity, to be ternary. That is, the beads can be either hydrophobic, neutral, or hydrophilic, and each is represented by the state variable as $\eta_i = 1, 0, -1$ (see the next section for more details). The interaction strength σ_{ij} is then determined by the hydrophobicities of the two monomers as

$$\sigma_{ij} = \begin{cases} -\varepsilon & \text{if } \eta_i = 1 \text{ and } \eta_j = 1, \\ 0 & \text{if } \eta_i = 0 \text{ or } \eta_j = 0, \\ \frac{2}{3}\varepsilon & \text{otherwise,} \end{cases} \tag{A5}$$

where ε is a key parameter determining the equilibrium conformations of FG Nups. The total energy of the system, consisting of only FG Nups, is given by $U = (1/2)\sum_{i\neq j} U_{ij}$ where i is the monomer index, running over all monomers in the system.

2. An inert cargo

Now let us introduce an inert cargo of radius R. Without bound TF, the cargo interacts only sterically with the

monomers constituting the FG Nups. This steric interaction between a cargo and a monomer has the same form as in Eq. (A2) but with $r_0 = R + a/2$, which we denote as ϕ^{st}_{cargo}.

3. An interacting cargo

Finally, we consider a cargo bound to a TF. When a cargo binds a TF, they form a cargo-TF complex, which we refer to as an interacting cargo. TFs, also called karyopherins, interact specifically with FG Nups. On its surface, a TF has multiple hydrophobic pockets that serve as binding spots for FG repeat domains of FG Nups. Taking this into account, we model an interacting cargo as a sphere with N_b discrete binding sites distributed in a stripe pattern (see Fig. 5). Another interesting characteristic of TFs is that they are more negatively charged than most of cellular proteins. For example, the charge (Q) of TFs in a human body at pH 7.2 lies in the range $-120e \leq Q \leq -20e$ [47]. We thus consider that a TF has negative charges of $Q = -60e$, evenly distributed on the binding spots. In this study, we choose $N_b = 12$, and each binding site therefore has a negative charge, $q = -5e$. In our study, the presence of TF is incorporated only via binding sites distributed on a cargo. Accordingly, we assume that the charge Q is distributed on the binding sites, but in reality, it is distributed over the entire TF. A more realistic description of the electrostatic effects will need to take into account the structure of the TF as well, which is an interesting direction to pursue.

Then, the pairwise interaction potential between the i-th monomer of FG Nups and the ℓ-th binding site of a TF is given by

$$U_{i\ell} = \phi^{st}(r_{i\ell}) + \phi^{Coul}_{i\ell}(r_{i\ell}) + \phi^{sp}_{i\ell}(r_{i\ell}), \qquad \text{(A6)}$$

where $r_{i\ell} = |\mathbf{r}_i - \mathbf{r}_\ell|$ with $\mathbf{r}_\ell$ being the position vector of the ℓ-th binding site of a TF. The last term, ϕ^{sp}, represents the specific interaction between a FG repeat and a cognate TF binding site, which occurs as the phenylalanine side chain of FG nup is inserted into a hydrophobic pocket on the surface of TF. As a surface interaction, a binding site (or hydrophobic pocket) interacts only with a single FG domain, not with several domains simultaneously. We incorporate this exclusive nature of the FG-TF interaction by turning on ϕ^{sp} only for the closest pairs of FG-containing monomers and TF binding sites, if the distance is less than $3a$. In addition, ϕ^{sp} is assumed to be given by the same short-range potential as in Eq. (A4), but with different interaction strength $\sigma_{i\ell} = -\varepsilon_{TF}$.

The total energy of the system consisting of FG nups and an interacting cargo is hence given by

$$U = \frac{1}{2}\sum_{i\neq j} U_{ij} + \sum_{i,\ell} U_{i\ell} + \phi^{st}_{cargo} \qquad \text{(A7)}$$

up to an irrelevant constant term due to interactions between binding sites in a single TF, where ϕ^{st}_{cargo} is the steric interaction between a cargo and a monomer in FG nups. Here, i runs over the monomer index, and ℓ over the binding site index.

4. Monte Carlo simulation

Using the Metropolis algorithm, we perform Monte Carlo simulations and update the configurations of the system. In the Metropolis algorithm, the probability for an update (or equivalently, a move) to be accepted satisfies the detailed balance condition

$$p_{\rm eq}(i)W(i \to j) = p_{\rm eq}(j)W(j \to i) \qquad \text{(A8)}$$

where i, j are configurations before and after the move, respectively. $p_{\rm eq}(x)$ is the equilibrium probability density of configuration x, and $W(x \to y)$ is the transition probability from x to y. In the simulation, the transition probability is given by $W(x \to y) = \pi(x \to y)\mathrm{acc}(x \to y)$, where $\pi(x \to y)$ is the probability to select the move and $\mathrm{acc}(x \to y)$ is the acceptance ratio. The Metropolis algorithm fulfills the detailed balance condition by using an acceptance ratio given by

$$\mathrm{acc}(i \to j) = \min\left(1, \frac{\pi(j \to i)}{\pi(i \to j)} e^{-\beta(E_j - E_i)}\right) , \qquad \text{(A9)}$$

where $\min(x, y)$ gives the lesser value between x and y, and $e^{-\beta(E_j - E_i)} = p_{\rm eq}(j)/p_{\rm eq}(i)$ is the ratio between the canonical equilibrium probability densities.

In order to effectively sample the configurations of the FJCs, various moves such as monomer rotation, pivot, crank, and pivot cluster moves are employed. The pivot cluster move (PCM) is newly developed in this study with the aim of efficiently sampling configurations of strongly bonded FJCs anchored at a wall. The PCM achieves this goal by first performing a rigid body motion for the strongly bonded monomers, and then deforming conformations of the rest of the chain with a number of pivot moves so that the connectivity condition of each chain and anchor to the wall are preserved. Step sizes of the moves were 6.28, 3.80, 6.28, 2.60, for monomer rotation, pivot, crank and pivot cluster respectively, where the units of first three are in radians and the last is in units of monomer diameter a. The acceptance ratios of the moves are 0.77, 0.37, 0.40, 0.30, in the same order. For cargos, the translation and rotation moves are used with step sizes of 1.17(in unit of a) and 6.28(in radian), and the resulting acceptance ratios are 0.35 and 0.95, respectively. The simulations typically run for $\mathcal{O}(10^6)$ Monte Carlo steps per monomer after $\sim 3 \times 10^5$ steps for the equilibration.

Appendix B: Coarse graining of amino acid sequences of FG nups

We consider a model NPC that is composed only of Nsp1. There exist a variety of FG nups constituting

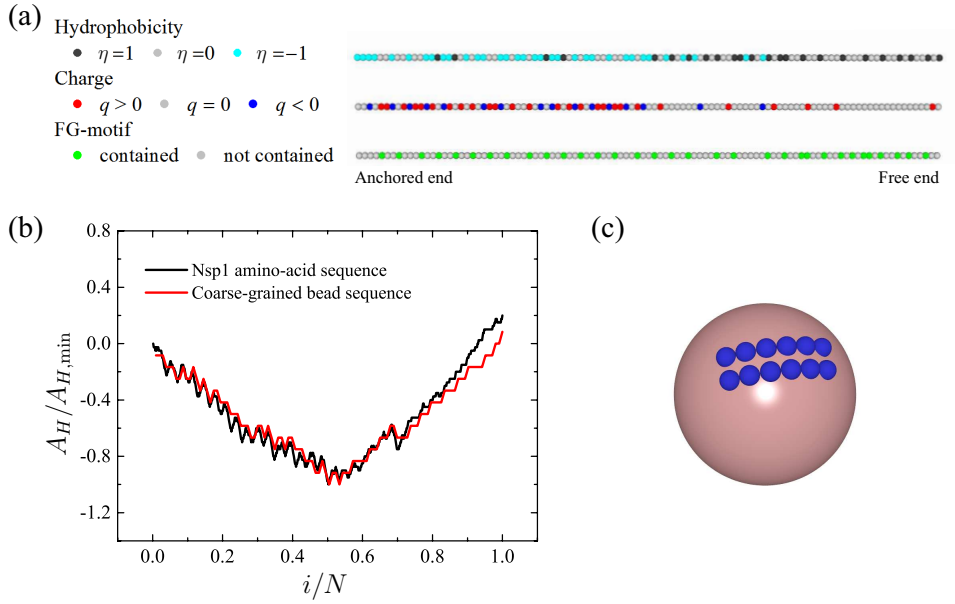

FIG. 5. (a) Hydrophobicity, charge, and FG-motif distributions on the monomers of a coarse-grained Nsp1. (b) Accumulated hydrophobicity $A_H(i) \equiv \sum_{j=1}^{i} \eta_j$, evaluated for the original amino acid sequence of Nsp1 (black line) and for the coarse-grained monomer sequence (red line), as function of the normalized bead index i/N. The numbers of beads are given as $N = 617$ for real Nsp1 and $N = 103$ for model Nsp1, respectively. The accumulated hydrophobicity is also normalized by the magnitude of its minimum value, $A_{H,\min}$. Bipartite nature of the hydrophobicity distribution is clearly shown; about half of beads toward the anchoring end are hydrophilic, while the other half of beads are hydrophobic. It also turns out that the distribution of hydrophobicity in the original sequence is preserved in coarse-grained FG nup. (c) Distribution of 12 binding sites for FG motifs on a cargo-TF complex. Binding sites are closely packed along two stripes beside a great circle on the spherical cargo. The distance between the stripes is set to $1.2a$.

NPCs, but Nsp1 is the most abundant yeast nucleoporin with biphasic characteristic where the cohesive globular domain is separated from stalk region [20]. Nsp1 consists of 617 amino acids, and the physical property of each amino acid is characterized by finite volume, electric charge and hydrophobicity. In order to save numerical cost, we group six amino acids to represent a single monomer in our coarse-grained model and represent their properties by the property of the monomer.

1. Charge and hydrophobicity

Charge and hydrophobicity of a monomer are assigned in the following way. Let i, α be indices to denote the α-th amino acid in the i-th group which is represented by the i-th monomer. Charge of the i-th monomer, q_i, is determined by the sum of $q_{i,\alpha}$, the charge of the α-th amino acid in the i-th monomer:

$$q_i = \sum_{\alpha=1}^{6} q_{i,\alpha} \ . \tag{B1}$$

According to the Honeycutt-Thirumulai model [39, 40], the hydrophobicity of the i-th monomer, η_i, can be $\eta_i = 1$ (hydrophobic), or $\eta_i = 0$ (hydrophobic neutral), or $\eta_i = -1$ (hydrophilic). These three values are chosen as

$$\eta_i = \begin{cases} 1 & \text{if } \langle \eta_{i,l} \rangle > \eta_u, \\ 0 & \text{if } \eta_l < \langle \eta_{i,l} \rangle < \eta_u, \\ -1 & \text{if } \langle \eta_{i,l} \rangle < \eta_l, \end{cases} \tag{B2}$$

where $\langle \eta_{i,\alpha} \rangle \equiv \sum_{\alpha=1}^{6} \eta_{i,\alpha}/6$ with $\eta_{i,\alpha}$ being the hydrophobicity of the α-th amino acid represented by the i-th monomer, and we set $\eta_u = 0.587$, $\eta_l = 0.3$. The threshold values η_u and η_l are assigned such that the portions of hydrophobic, neutral, and hydrophilic beads of the coarse-grained FG nup coincide with the respective portions of the amino-acids of Nsp1. The hydrophobicity of the individual amino-acid, $\eta_{i,\alpha}$, is given by the values at TABLE S2 in Supporting information of Ref. [26]. The amino-acid is classified as hydrophobic if $\eta_{i,\alpha}$ is higher than 0.66, hydrophilic if $\eta_{i,\alpha}$ is lower than 0.33, and otherwise, neutral.

Following the scheme explained above, we perform a coarse graining of amino acids in Nsp1. Shown in Fig. 5(a) is the result where the distributions of hydrophobicity, electric charge, and FG-domains are depicted along the monomers in the coarse-grained FG nup. The anchoring ends are strongly charged and hydrophilic, and the free ends are weakly charged and hydrophobic, which bears a close resemblance to the charge and hydrophobicity profiles of the original amino acid sequences.

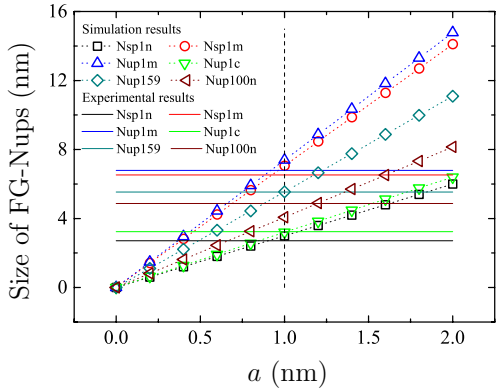

FIG. 6. Radii of gyration for various coarse-grained FG nups as a function of the monomer size a. We set the hydrophobic interaction strength to be $\varepsilon = 1.7$. For all FG nups examined here, when a is taken to be 1nm, radii of gyration of various FG nups are compatible with experimentally-measured Stokes radii. In simulations, the radius of the pore is set to be $R_{pore} = 25a$, yielding $R_{pore}/R_g(\text{Nsp1m}) = 3.55$, which is in reasonable accordance with experimental values, 3.83.

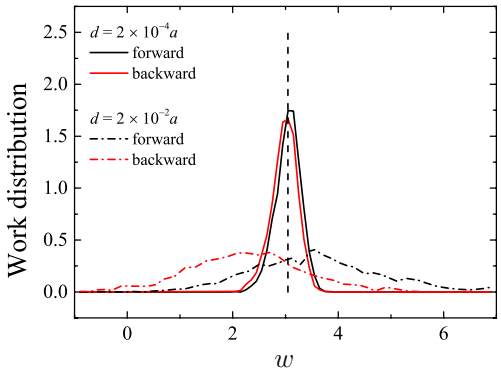

FIG. 7. Probability distributions of work done by moving an inert cargo with radius $R = 6a$ from $z_0 = -40a$ to $z = 0$ (see Fig. 2(a) and related explanation in main text). The vertical dashed line is the free energy difference estimated through Eq. (C6). At the estimated free energy difference, the work distribution from the forward process, $p_f(w)$ (black lines) intersects with the distribution of negative work from the corresponding backward process, $p_b(-w)$ (red lines). This confirms the validity of the estimated ΔF.

2. Radius of gyration of FG nup

Using our coarse-graining scheme, we calculate, from simulations, the radii of gyration of various FG nups that are different in lengths and sequential arrangements of amino acids. The radius of gyration is linearly proportional to the monomer size a which is taken in this work as a unit length. When compared with experimental measurement, the radius of gyration can, therefore, be used to infer the value of a. The results are shown in Fig. 6 where the symbols represent the simulation data for different FG nups and the horizontal lines are the Stokes radii measured for the FG nups in an experiment by Yamada *et. al.* [20]. Here we set $\varepsilon = 1.7$ (see the main text). When a is taken to be about 1nm, the radii of gyration of FG nups show consistent results with experimental values of the Stokes radii. Of course, the radius of gyration is different from the Stokes radius but can be derived, in principle, by appropriate rescaling of the measured Stokes radius if a specific object shape is considered. For simplicity, we assume here the scaling factor of 1.0 for approximately globular proteins. We note, however, that all lengths in our simulations are rescaled in units of a so that a specific value of a does not lead to qualitative changes in the major results drawn here.

Appendix C: Method of free energy estimation

We explain how free energy profiles $F(z) - F(z_0) = \Delta F(z)$ of FG nups as a function of cargo position z is calculated by using the Jarzynski equality. Let z denote the position of cargo (FG nups are anchored at a surface, $z = 0$). We consider a process to move the cargo position from z_0 to z following a stepwise sequence,

$$z_n = z_0 + nd, \quad n = 0, 1, \cdots M \tag{C1}$$

with the step size $d = (z - z_0)/M$. At the zeroth step ($n = 0$), the cargo is located at z_0. As the move is repeated (or as n increases), the cargo approaches toward the anchoring surface of FG nups. At the final Mth step, the cargo reaches its designated position z at which $F(z)$ is evaluated.

During the process, due to the interaction between the cargo and FG nups, finite work w should be expended:

$$w = \sum_{n=0}^{M-1} \left[U(s_n, z_{n+1}) - U(s_n, z_n)\right] \ , \tag{C2}$$

where s_n represents the configuration of FG nups with the cargo located at z_n. Here, $U(s, z)$ is given by Eq. (A7) for FG nups having configuration s and for the cargo positioned at z (for an inert cargo, the second term in Eq. (A7) is zero).

Crooks proved that w given as above satisfies the Jarzynski relation [41, 42]:

$$\int_{-\infty}^{\infty} dw p_f(w) e^{-\beta w} = \langle e^{-\beta w} \rangle = e^{-\beta \Delta F(z)}, \tag{C3}$$

where $\beta^{-1} = k_B T$, and $p_f(w)$ is the probability distribution function of w. The above equality is in fact an integral version of the following relation [43]:

$$p_f(w) e^{-\beta w} = e^{-\beta \Delta F} p_b(-w). \tag{C4}$$

Here $p_b(w)$ is the probability distribution function of w obtained from the reversed process of Eq.(C1):

$$\tilde{z}_n = z - nd, \quad n = 0, 1, \cdots, M, \tag{C5}$$

which corresponds to move a cargo from z to z_0 ($\tilde{z}_0 = z$ and $\tilde{z}_M = z_0$). Integrating the above equation (C4) with respect to w, one obtains Eq. (C3) for the normalized probability distribution $p_b(-w)$. Note here that $p_f(w)$ and $p_b(-w)$ cross with each other at $w = \Delta F$.

Performing MC simulations, we record the energy differences made in every step of n, the summand of Eq. (C2), for a certain cargo position z. The initial location is chosen as $z_0 = -40a$ for any z. From a single run of MC simulation, we acquire a certain work value w_i and obtain the free energy difference, following Eq. (C3):

$$-\ln\left[\frac{1}{N_{run}}\sum_{i=1}^{N_{run}} e^{-\beta w_i}\right] = \beta\Delta F(z_F) \qquad \text{(C6)}$$

from $N_{run} = 100 \sim 1000$ independent MC simulations. The validity of the estimated free energy difference can be confirmed by the Crooks relation (C4). We obtain the probability distributions of work, $p_f(w)$ and $p_b(-w)$ to check whether their crossing point coincides with $\Delta F(z_F)$ estimated from Eq. (C6).

Figure 7 shows an example of the free energy estimation and its validity check. The lines are the probability distribution of work obtained in our simulations. Taking average of $e^{-\beta w}$ gives ΔF, according to Eq. (C3). For small step size, $d = 2 \times 10^{-4}a$, the distribution is very narrow and is centered around $w = 3$, and the estimated $\Delta F = 3.038$ (vertical dashed line) is almost identical to the most probable value of w. For large step size $d = 2 \times 10^{-2}$, the distributions become wider, but the intersection point between the work distributions from the forward and the backward process is pinned at $w = \Delta F \approx 3$. This confirms the Crooks relation (C4) and also the validity of the estimated value of free energy difference.

Appendix D: Free energy landscapes

In Fig 8, we present NPC free energy landscapes obtained for cargos of various sizes and interaction strengths. For small cargos($R = 2$), the height of the free energy barrier is similar to or smaller than the thermal energy scale k_BT, so that inert cargos can easily overcome the barrier with thermal fluctuation. Binding of transport factors only form an energy well and slow down the transport process. Meanwhile for large cargos, the model NPC is impermeable as the height of the free energy barrier is much larger than the thermal energy scale. The model NPC, however, can be turned into a permeable gate if a transport factor is attached to the cargo forming a cargo-TF complex, whereupon the transport process can be accelerated with the cooperation of RanGTP, which pumps out the cargo-TF complex from *trans* side.

Appendix E: Effect of RanGTP

Figure 9 presents transport diagrams for various values of k, illustrating the effect of RanGTP. For all k values, the boundaries separating the permeable and impermeable regions are identical to one another. The effect of RanGTP only appears in the diagrams for $k = 10^3, 10^4$, where the fast region expands compared to the case $k = 0$. There is no noticeable difference between the diagrams for $k = 0$ and $k = 10^2$. Also one can see that the effect of RanGTP is saturated for $k > 10^3$, given the similarity between the cases of $k = 10^3$ and $k = 10^4$.

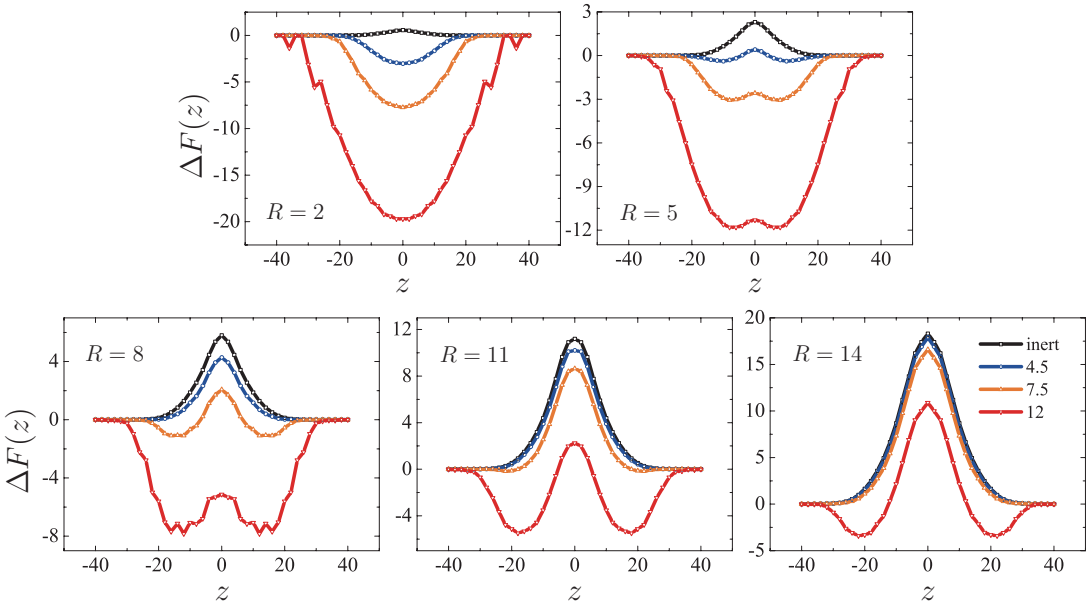

FIG. 8. The free energy landscapes for cargos of various sizes and interaction strengths.

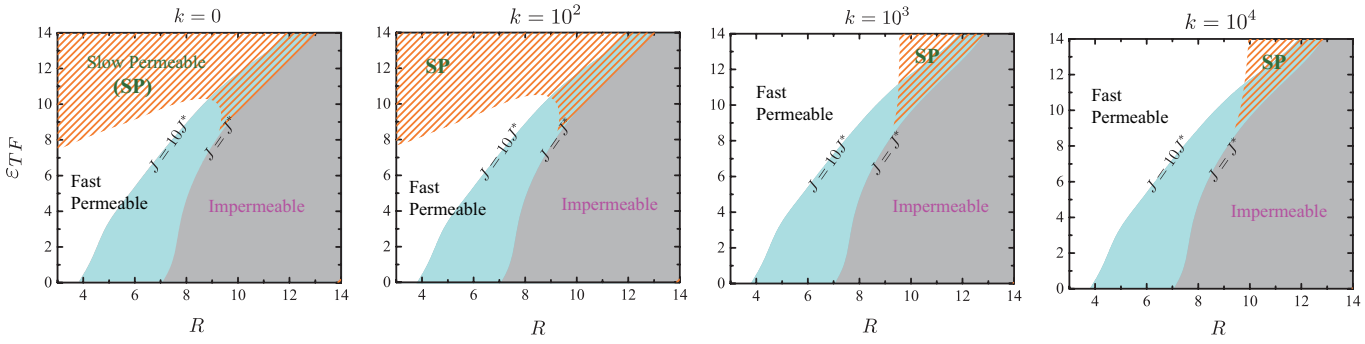

FIG. 9. The same diagrams with Fig. 4 of the main text, indicating distinct transport regimes for various values of k. Difference between the diagrams for $k = 0$ and $k = 10^2$ is hardly appreciable. Also for the case of $k = 10^4$, each region in the diagram is almost the same as that for $k = 10^3$ case.

[1] J. Fernandez-Martinez and M. P. Rout, "A jumbo problem: mapping the structure and functions of the nuclear pore complex," Curr. Opin. Cell Biol. **24**, 92 (2012).

[2] H. B. Schmidt and D. Grlich, "Transport selectivity of nuclear pores, phase separation, and membraneless organelles," Trends Biochem. Sci. **41**, 46 (2016).

[3] F. Alber, S. Dokudovskaya, L. M. Veenhoff, W. Zhang, J. Kipper, D. Devos, A. Suprapto, O. Karni-Schmidt, R. Williams, B. T. Chait, *et al.*, "Determining the architectures of macromolecular assemblies," Nature (London) **450**, 683 (2007).

[4] F. Alber, S. Dokudovskaya, L. M. Veenhoff, W. Zhang, J. Kipper, D. Devos, A. Suprapto, O. Karni-Schmidt, R. Williams, B. T. Chait, *et al.*, "The molecular architecture of the nuclear pore complex," Nature (London) **450**, 695 (2007).

[5] A. R. Lowe, J. J. Siegel, P. Kalab, M. Siu, K. Weis, and J. T. Liphardt, "Selectivity mechanism of the nuclear pore complex characterized by single cargo tracking," Nature (London) **467**, 600 (2010).

[6] D. Grünwald and R. H. Singer, "In vivo imaging of labelled endogenous β-actin mRNA during nucleocytoplasmic transport," Nature (London) **467**, 604 (2010).

[7] J. Ma, A. Goryaynov, A. Sarma, and W. Yang, "Self-regulated viscous channel in the nuclear pore complex," Proc. Natl. Acad. Sci. U.S.A. **109**, 7326 (2012).

[8] L.-C. Tu, G. Fu, A. Zilman, and S. M. Musser, "Large cargo transport by nuclear pores: implications for the spatial organization of fg-nucleoporins," EMBO J. **32**, 3220 (2013).

[9] M. P. Rout, J. D. Aitchison, A. Suprapto, K. Hjertaas, Y. Zhao, and B. T. Chait, "The yeast nuclear pore complex," J. Cell Biol. **148**, 635 (2000).

[10] M. P. Rout, J. D. Aitchison, M. O. Magnasco, and B. T. Chait, "Virtual gating and nuclear transport: the hole picture," Trends Cell Biol. **13**, 622 (2003).

[11] R. Y. H. Lim, N.-P. Huang, J. K?ser, J. Deng, K. H. A. Lau, K. Schwarz-Herion, B. Fahrenkrog, and U. Aebi, "Flexible phenylalanine-glycine nucleoporins as entropic barriers to nucleocytoplasmic transport," Proc. Natl. Acad. Sci. U.S.A. **103**, 9512 (2006).

[12] S. Frey, R. P. Richter, and D. Görlich, "Fg-rich repeats of nuclear pore proteins form a three-dimensional meshwork with hydrogel-like properties," Science **314**, 815 (2006).

[13] S. Frey and D. Görlich, "A saturated fg-repeat hydrogel can reproduce the permeability properties of nuclear pore complexes," Cell **130**, 512 (2007).

[14] C. Ader, S. Frey, W. Maas, H. B. Schmidt, D. Görlich, and M. Baldus, "Amyloid-like interactions within nucleoporin fg hydrogels," Proc. Natl. Acad. Sci. U.S.A. **107**, 6281 (2010).

[15] K. Ribbeck and D. Görlich, "Kinetic analysis of translocation through nuclear pore complexes," EMBO J. **20**, 1320 (2001).

[16] K. Ribbeck and D. Görlich, "The permeability barrier of nuclear pore complexes appears to operate via hydrophobic exclusion," EMBO J. **21**, 2664 (2002).

[17] R. Y. Lim, B. Fahrenkrog, J. Köser, K. Schwarz-Herion, J. Deng, and U. Aebi, "Nanomechanical basis of selective gating by the nuclear pore complex," Science **318**, 640 (2007).

[18] R. L. Schoch, L. E. Kapinos, and R. Y. Lim, "Nuclear transport receptor binding avidity triggers a self-healing collapse transition in fg-nucleoporin molecular brushes," Proc. Natl. Acad. Sci. U.S.A. **109**, 16911 (2012).

[19] R. Peters, "Translocation through the nuclear pore complex: selectivity and speed by reduction-of-dimensionality," Traffic **6**, 421 (2005).

[20] J. Yamada, J. L. Phillips, S. Patel, G. Goldfien, A. Calestagne-Morelli, H. Huang, R. Reza, J. Acheson, V. V. Krishnan, S. Newsam, *et al.*, "A bimodal distribution of two distinct categories of intrinsically disordered structures with separate functions in fg nucleoporins," Mol. Cell. Proteomics **9**, 2205 (2010).

[21] T. Bickel and R. Bruinsma, "The nuclear pore complex mystery and anomalous diffusion in reversible gels," Biophys. J. **83**, 3079 (2002).

[22] T. Kustanovich and Y. Rabin, "Metastable network model of protein transport through nuclear pores," Biophys. J. **86**, 2008 (2004).

[23] J. S. Mincer and S. M. Simon, "Simulations of nuclear pore transport yield mechanistic insights and quantitative predictions," Proc. Natl. Acad. Sci. U.S.A. **108**, E351 (2011).

[24] M. Tagliazucchi, O. Peleg, M. Kröger, Y. Rabin, and I. Szleifer, "Effect of charge, hydrophobicity, and sequence of nucleoporins on the translocation of model particles through the nuclear pore complex," Proc. Natl. Acad. Sci. U.S.A. **110**, 3363 (2013).

[25] A. Ghavami, E. van der Giessen, and P. R. Onck, "Energetics of transport through the nuclear pore complex," PLoS one **11**, e0148876 (2016).

[26] A. Ghavami, L. M. Veenhoff, E. van der Giessen, and P. R. Onck, "Probing the disordered domain of the nuclear pore complex through coarse-grained molecular dynamics simulations," Biophys. J. **107**, 1393 (2014).

[27] D. Ando, R. Zandi, Y. W. Kim, M. Colvin, M. Rexach, and A. Gopinathan, "Nuclear pore complex protein sequences determine overall copolymer brush structure and function," Biophys. J. **106**, 1997 (2014).

[28] L. Miao and K. Schulten, "Probing a structural model of the nuclear pore complex channel through molecular dynamics," Biophys. J. **98**, 1658 (2010).

[29] R. Moussavi-Baygi, Y. Jamali, R. Karimi, and M. R. Mofrad, "Brownian dynamics simulation of nucleocytoplasmic transport: a coarse-grained model for the functional state of the nuclear pore complex," PLoS Comput. Biol. **7**, e1002049 (2011).

[30] D. Osmanovic, J. Bailey, A. H. Harker, A. Fassati, B. W. Hoogenboom, and I. J. Ford, "Bistable collective behavior of polymers tethered in a nanopore," Phys. Rev. E **85**, 061917 (2012).

[31] A. Zilman, S. Di Talia, B. T. Chait, M. P. Rout, and M. O. Magnasco, "Efficiency, selectivity, and robustness of nucleocytoplasmic transport," PLoS Comput. Biol. **3**, e125 (2007).

[32] B. Raveh, J. M. Karp, S. Sparks, K. Dutta, M. P. Rout, A. Sali, and D. Cowburn, "Slide-and-exchange mechanism for rapid and selective transport through the nuclear pore complex," Proc. Natl. Acad. Sci. U.S.A. **113**, E2489 (2016).

[33] T. Jovanovic-Talisman, J. Tetenbaum-Novatt, A. S. McKenney, A. Zilman, R. Peters, M. P. Rout, and B. T. Chait, "Artificial nanopores that mimic the transport selectivity of the nuclear pore complex," Nature (London) **457**, 1023 (2009).

[34] S. W. Kowalczyk, L. Kapinos, T. R. Blosser, T. Magalhães, P. Van Nies, R. Y. Lim, and C. Dekker, "Single-molecule transport across an individual biomimetic nuclear pore complex," Nat. Nanotech. **6**, 433 (2011).

[35] L. A. Strawn, T. Shen, N. Shulga, D. S. Goldfarb, and S. R. Wente, "Minimal nuclear pore complexes define fg repeat domains essential for transport." Nat. Cell Biol. **6**, 197 (2004).

[36] Y. Sakiyama, A. Mazur, L. E. Kapinos, and R. Y. Lim, "Spatiotemporal dynamics of the nuclear pore complex transport barrier resolved by high-speed atomic force microscopy," Nat. Nanotech. **11**, 719 (2016).

[37] W. Sung and P. Park, "Polymer translocation through a pore in a membrane," Phys. Rev. Lett. **77**, 783 (1996).

[38] A. Gopinathan and Y. W. Kim, "Polymer translocation in crowded environments," Phys. Rev. Lett. **99**, 228106 (2007).

[39] J.-E. Shea, Y. D. Nochomovitz, Z. Guo, and C. L. Brooks III, "Exploring the space of protein folding hamiltonians: The balance of forces in a minimalist β-barrel model," J. Chem. Phys. **109**, 2895 (1998).

[40] J. Honeycutt and D. Thirumalai, "Metastability of the folded states of globular proteins," Proc. Natl. Acad. Sci. U.S.A. **87**, 3526 (1990).

[41] C. Jarzynski, "Nonequilibrium equality for free energy differences," Phys. Rev. Lett. **78**, 2690 (1997).

[42] G. E. Crooks, "Nonequilibrium measurements of free energy differences for microscopically reversible markovian systems," J. Stat. Phys. **90**, 1481 (1998).

[43] G. E. Crooks, "Entropy production fluctuation theorem and the nonequilibrium work relation for free energy differences," Phys. Rev. E **60**, 2721 (1999).

[44] Numerical solution of the Fokker-Planck equation is obtained by using the commercial software WOLFRAM MATHEMATICA which automatically selects method among typical techniques for solving ordinary differential equation, e.g., explicit Runge-Kutta method (http://www.wolfram.com).

[45] J. Liphardt, S. Dumont, S. B. Smith, I. Tinoco, and C. Bustamante, "Equilibrium information from nonequilibrium measurements in an experimental test of jarzynski9s equality," Science **296**, 1832 (2002).

[46] D. Collin, F. Ritort, C. Jarzynski, S. B. Smith, I. Tinoco, and C. Bustamante, "Verification of the crooks fluctuation theorem and recovery of rna folding free energies," Nature (London) **437**, 231 (2005).

[47] L. J. Colwell, M. P. Brenner, and K. Ribbeck, "Charge as a selection criterion for translocation through the nuclear pore complex," PLoS Comput. Biol. **6**, e1000747 (2010).

[48] S. K. Lyman, T. Guan, J. Bednenko, H. Wodrich, and L. Gerace, "Influence of cargo size on ran and energy requirements for nuclear protein import," J. Cell Biol. **159**, 55 (2002).

[49] K. Lott, A. Bhardwaj, G. Mitrousis, N. Pante, and G. Cingolani, "The importin β binding domain modulates the avidity of importin β for the nuclear pore complex," J. Biol. Chem. **285**, 13769 (2010).

[50] J. Tetenbaum-Novatt, L. E. Hough, R. Mironska, A. S. McKenney, and M. P. Rout, "Nucleocytoplasmic transport: a role for nonspecific competition in karyopherin-nucleoporin interactions," Mol. Cell. Proteomics **11**, 31 (2012).

[51] T. A. Isgro and K. Schulten, "Binding dynamics of isolated nucleoporin repeat regions to importin-β," Structure **13**, 1869 (2005).

[52] M. Doi and S. F. Edwards, *The Theory of Polymer Dynamics* (oxford university press, 1986).

[53] B. Alberts, *Molecular Biology of the Cell* (Garland Science, 2008).

[54] W. Yang and S. M. Musser, "Nuclear import time and transport efficiency depend on importin β concentration," J. Cell Biol. **174**, 951 (2006).

[55] W. Yang, J. Gelles, and S. M. Musser, "Imaging of single-molecule translocation through nuclear pore complexes", Proc. Natl. Acad. Sci. U.S.A. **101**, 12887 (2004).

[56] I. G. Macara, "Transport into and out of the Nucleus", Microbiol. Mol. Biol. Rev. **65**, 570 (2001).

[57] The threshold value of k as well as the on-rate k_{on} increase if a smaller value of τ^* is chosen. For example, if $\tau^* = 1$ msec is used, the threshold value of k lies between 10^3 and 4×10^3.

[58] D. Görlich, M. J. Seewald, and K. Ribbeck, "Characterization of ran-driven cargo transport and the rangtpase system by kinetic measurements and computer simulation," EMBO J. **22**, 1088 (2003).

[59] D. Gilchrist, B. Mykytka, and M. Rexach, "Accelerating the rate of disassembly of karyopherin· cargo complexes," J. Biol. Chem. **277**, 18161 (2002).

[60] A. R. Lowe, J. H. Tang, J. Yassif, M. Graf, W. Y. Huang, J. T. Groves, K. Weis, and J. T. Liphardt, "Importin-β modulates the permeability of the nuclear pore complex in a ran-dependent manner," eLife **4**, e04052 (2015).

[61] L. E. Kapinos, B. Huang, C. Rencurel, and R. Y. Lim, "Karyopherins regulate nuclear pore complex barrier and transport function," J. Cell Biol. (2017), 10.1083/jcb.201702092.

[62] C. W. Akey and M. Radermacher, "Architecture of the xenopus nuclear pore complex revealed by three-dimensional cryo-electron microscopy," J. Cell Biol. **122**, 1 (1993).

[63] A. Bestembayeva, A. Kramer, A. A. Labokha, D. Osmanović, I. Liashkovich, E. V. Orlova, I. J. Ford, G. Charras, A. Fassati, and B. W. Hoogenboom, "Nanoscale stiffness topography reveals structure and mechanics of the transport barrier in intact nuclear pore complexes," Nat. Nanotech. **10**, 60 (2015).

[64] A. Vovk, C. Gu, M. G. Opferman, L. E. Kapinos, R. Y. Lim, R. D. Coalson, D. Jasnow, and A. Zilman, "Simple biophysics underpins collective conformations of the intrinsically disordered proteins of the nuclear pore complex," eLife **5**, e10785 (2016).

[65] A. Eskandari Nasrabad, D. Jasnow, A. Zilman, and R. D. Coalson, "Precise control of polymer coated nanopores by nanoparticle additives: Insights from computational modeling," J. Chem. Phys. **145**, 064901 (2016).

[66] R. Zahn, D. Osmanović, S. Ehret, C. A. Callis, S. Frey, M. Stewart, C. You, D. Görlich, B. W. Hoogenboom, and R. P. Richter, "A physical model describing the interaction of nuclear transport receptors with fg nucleoporin domain assemblies," eLife **5**, e14119 (2016).

[67] D. Ando and A. Gopinathan, "Cooperative interactions between different classes of disordered proteins play a functional role in the nuclear pore complex of baker's

yeast," PLoS one **12**, e0169455 (2017).
[68] M. Isobe, H. Shimizu, and Y. Hiwatari, "A multicanonical molecular dynamics study on a simple bead-spring model for protein folding," J. Phys. Soc. Japan **70**, 1233 (2001).